Ultrasonic Nondestructive Evaluation of Additively Manufactured Wear Coatings

Ziyad Smoqi[1]*, Luz D. Sotelo[1,2] Aniruddha Gaikwad[1], Joseph A. Turner[1], Prahalada Rao[1,3]

[1]Mechanical and Materials Engineering, University of Nebraska-Lincoln, Lincoln, NE, United States

[2]NAS-NRC Research Associate, U.S. Naval Research Laboratory, Code 7165, Washington, D.C., 20375, United States

[3]Grado Department of Industrial and Systems Engineering, Virginia Tech, Blacksburg, VA, United States

Corresponding author, email: zsmoqi@huskers.unl.edu

Abstract

This work pertains to the nondestructive evaluation of additively deposited coatings using ultrasound measurements. The specific objective was to evaluate the quality of Stellite 21 coatings deposited on Inconel 718 substrates by the directed energy deposition (DED) additive manufacturing (AM) process using ultrasound surface wave measurements. The surface wave speed and diffuse backscatter amplitude of the ultrasound waves were correlated with both cracking and warpage of the coating. This research is important because the integrity of DED-processed coatings currently requires a combination of destructive metallographic studies and X-ray computed tomography analysis, which are both expensive and time consuming. Instead of using a normal incidence configuration for the ultrasound measurements, the surface-wave approach allows the inspection of the near surface coating integrity. Three different frequencies were used to excite surface waves because each frequency has a different penetration depth. The signals obtained were used to quantify and compare the surface wave speed and surface wave-diffuse ultrasonic backscatter amplitude from five different DED-processed Stellite coated samples. Considering destructive metallurgical characterization as a reference, surface wave measurements were found to be effective for examining coating integrity; the backscatter amplitude of the surface waves was correlated with the crack density and warpage. These flaws also change the stress state of the Stellite coating and consequently the surface wave propagation speed and its scattering behavior.

Keywords: *Nondestructive Characterization; Ultrasonic Surface Waves; Stellite Coating; Directed Energy Deposition; Additive Manufacturing; Cracking and Warpage.*

1 Introduction

1.1 Motivation and Background

In this work we evaluate the quality of additively deposited coatings using nondestructive ultrasound measurements. The specific objective was to evaluate through ultrasound surface wave measurements the quality of Stellite 21 wear coatings deposited on Inconel 718 substrates by the directed energy deposition (DED) additive manufacturing process. In DED parts are built layer-by-layer by depositing powder material from four nozzles, which is fused using a high-power laser [1-3]. The process is particularly beneficial in repair and near-net shape applications. A schematic of the DED process is shown in Figure 1.

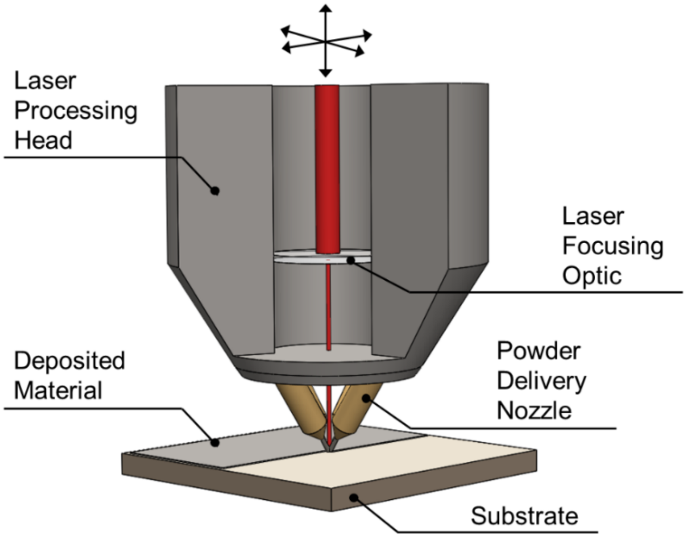

Figure 1: Schematic representation of directed energy deposition (DED) process. Material is sprayed from four nozzles and fused by the thermal energy supplied by a laser.

Despite the demonstrated potential of DED to transcend the design and processing barrier of traditional manufacturing, the tendency of the process to create flaws, such as porosity, cracking, segregation of detrimental phases, and nonuniformity of microstructure, hinders its broader adoption [4-9]. Therefore, nondestructive evaluation of DED-processed parts is an area of active research [10, 11]. Currently, most DED-processed parts are evaluated using destructive metallurgical analysis. Although X-ray computed tomography (XCT) is widely used to characterize additively manufactured parts nondestructively, high density materials such as stainless steels and Ni-super alloys limit the penetration depth of the X-rays. For example, for stainless steel parts a maximum penetration depth of ~10 mm and voxel resolution of 20 µm is achieved with an industrial XCT system operating at 225 kV. With this resolution, it is not possible to discern flaws less than 40 µm in diameter reliably [12]. Additionally, XCT does not provide information regarding the microstructure of the sample.

As an alternative nondestructive evaluation approach, ultrasound measurements are capable of acquiring information about the microstructure and physical flaws, such as porosity and cracking [5, 13-18]. Ultrasound measurements employ high-frequency sound waves (>20 kHz) to test and evaluate materials nondestructively [15]. The ultrasound phase velocity measurements are correlated to the elastic properties and microstructure of materials due to the dependence of wave speed on crystallographic orientation [19, 20]. In addition, in polycrystalline materials, the ultrasonic scattering and attenuation are linked with microstructural morphology and orientation [21-23]; while the diffuse ultrasonic backscatter (i.e., grain noise), which results from microstructure scattering, has been correlated to the grain size and grain size distribution [24].

1.2 Prior Work

Ultrasound measurements have been used extensively in evaluation of welds [25-29]. However, the use of ultrasound for quality assurance in metal additive manufacturing (AM) is challenging due to the large size and multi-layer nature of the process which can attenuate ultrasound significantly. Notably, Huang et al. [17] correlated the ultrasound wave speed to grain size and porosity in stainless steel 316L parts made using the binder jetting process. They further correlated the wave speed with mechanical properties (ductility and tensile strength), thus demonstrating the utility of ultrasound inspection for detecting not only flaw formation, but also for the prediction of mechanical properties.

Ultrasound measurements have also been used to characterize the quality of AM-processed polymers and composite materials. For example, Machado et al. [30] used an ultrasound technique to detect defects, such as voids, in samples made of different polymeric materials and composites produced by fused deposition modeling. Similarly, Zamen et al. [31] used nonlinear analysis of ultrasound signatures to characterize weak inter-layer bonding in large-scale AM polymers.

Furthermore, Bozek et al. [32] used nonlinear resonance ultrasonic spectroscopy (NRUS) for the nondestructive evaluation of AM parts. The authors predicted the fatigue life of Ti-6Al-4V cylindrical samples made using laser powder bed fusion additive manufacturing as a function of NRUS-related parameters, such as resonance frequency, quality factor, and hysteresis. In a different research study, Sotelo et. al. [13] employed linear ultrasound measurements to characterize the microstructure and elastic properties of 420 stainless steel samples built using DED. Similarly, Slotwinski et. al. [33] and Kim et al. [34] correlated the ultrasonic measurements with the degree of porosity in parts produced by laser powder bed fusion.

Recent studies have highlighted the potential of laser-generated ultrasound surface waves as a nondestructive method for microstructure characterization [20] and defect detection [34-37] in additively manufactured parts. Relatedly, Bakre et al. [38] used a surface ultrasonic waves in a contact wedge setup to obtain linear and nonlinear Rayleigh wave measurements, including wave speed, attenuation, and relative nonlinearity parameter, from as-printed, and re-melted directed energy deposition Ti6Al4V samples. An emerging area of research is the use of ultrasound measurements for in-process monitoring and closed-loop feedback control of AM processes [15, 18, 39, 40]. For example, Rieder et al. [18] installed an ultrasound transducer below the build platform and demonstrated that the longitudinal ultrasound waves captured void formation in-situ during processing.

1.3 Scope, Novelty, and Challenges

In our previous work [41], we deposited Stellite 21 coatings on Inconel 718 substrates. Stellite is a CoCr alloy used commonly as a wear coating [42-45]. Some of the typical applications of Stellite include wear and corrosion-resistant coatings on automotive valve seating surfaces, tools, gun barrels, and steam turbines [3, 44, 46-49]. The DED process enables deposition of Stellite on free-form surfaces in a uniform manner with reduced thermal-induced damage in comparison with wire-arc cladding. Deposition of Stellite coatings is challenging because the sample tends to generate near sub-surface cracks, heat-affected zones and spatially heterogeneous microstructure. Therefore, successful evaluation using nondestructive ultrasound waves will advance the application of DED-processed parts, including coatings, by minimizing the time spent on extensive sample preparation for destructive characterization. While the prior work in Ref. [41] investigates optimal processing conditions for crack-free deposition of Stellite 21 coatings on Inconel 718 substrates, the current work is dedicated towards nondestructive evaluation of these coatings using ultrasound techniques to preclude tedious, resource-intensice, and time consuming X-ray computed tomography characterization.

While ultrasound inspection of samples in AM is a topic of active research, the majority of studies use normal incidence ultrasound measurements [14, 15, 50] for which the waves propagate perpendicular to the surface of the sample. This approach is often used as a general practice to detect defects and to measure bulk elastic properties of AM processed metal parts. However, inspection of the microstructure and near-surface flaws, particularly for thin coatings, is difficult using this approach due to the presence of front-wall and back-wall reflections [51, 52]. Furthermore, the sensitivity of a normal incidence measurement is adversely affected by the orientation of flaws inside the coating. As a result, in normal incidence ultrasound, flaws oriented along the wave propagation path are difficult to detect. To address these challenges with normal incidence ultrasound, we use ultrasound surface wave measurements over three frequencies (7.5, 10, and 15 MHz) as an alternative to normal incidence [53, 54].

This article is organized as follows. Sec. 2 details the methodology, encompassing the DED processing of samples, experimental setup for ultrasound surface wave measurements, theoretical calculations of surface wave values, and calibration of the setup. Sec. 3 describes the results, including correlation of wave speed and diffuse backscatter amplitude with coating quality. Conclusion and avenues for future work are summarized in Sec. 4.

2 Methodology

2.1 Directed Energy Deposition Experiments

Stellite 21 coatings were deposited on individual Inconel 718 substrates (38 mm × 38 mm × 5.5 mm thick). The samples were deposited using an Optomec LENS MTS 500 controlled atmosphere hybrid DED system. To investigate the effect of substrate temperature and deposition laser power on the quality of Stellite 21 coatings, two process parameters were varied: the preheat laser power (P_h) and deposition laser power (P_d).

A schematic of the process, shown in Figure 2(a), illustrates the preheating process of the substrate and the deposition process of the coating. For preheating, the laser makes a pass on the substrate prior to deposition. The process conditions are summarized in Table 1, and the sample nomenclature for the five combinations of deposition and preheat laser power are listed in Table 2. Further details on DED processing of these samples, including a schematic and experimental setup, are available in Ref. [41].

Table 1: Process parameters used in DED of Stellite 21 on Inconel 718 [41].

Process Step	Laser Power P [W]	Scanning/ Deposition Pattern	Scan Velocity V[mm/s]	Hatch Spacing H [mm]	Layer Thickness T [mm]
Preheat (2 passes)	P_h = 0, 350, 400	Rectilinear, 0.70 mm distance between hatches	5.1	0.7 (= laser spot size (d))	N/A
Deposition (12 layers)	P_d = 200, 225, 275	Rectilinear, 95% overlap between hatches	10.6	0.375 (1.5 × T)	0.25

Table 2: Sample nomenclature used to describe the deposition condition of Stellite coatings studied in this work.

Sample Name	Preheat Laser Power, P_h [W]	Deposition Laser Power, P_d [W]
F	0	275
O	400	
P	0	225
Q	400	
N	350	200

Samples (10 mm x 10 mm x 6.5 mm) were cut using wire-electro discharge machining (wire-EDM). These were mechanically ground successively using (400, 600, 800, and 1200 grit) SiC sandpaper and polished using diamond paste (3, 1, and 0.5 µm). Finally, the samples were etched by swabbing with aqua regia (HCL: HNO_3=3:1) for approximately 10 seconds followed by dipping in water. In addition to the coating surface, both the transverse and longitudinal cross sections were processed in the above manner, as shown in Figure 2(b). The longitudinal cross section is parallel to the direction of the preheat laser path while the transverse cross section is normal to this path.

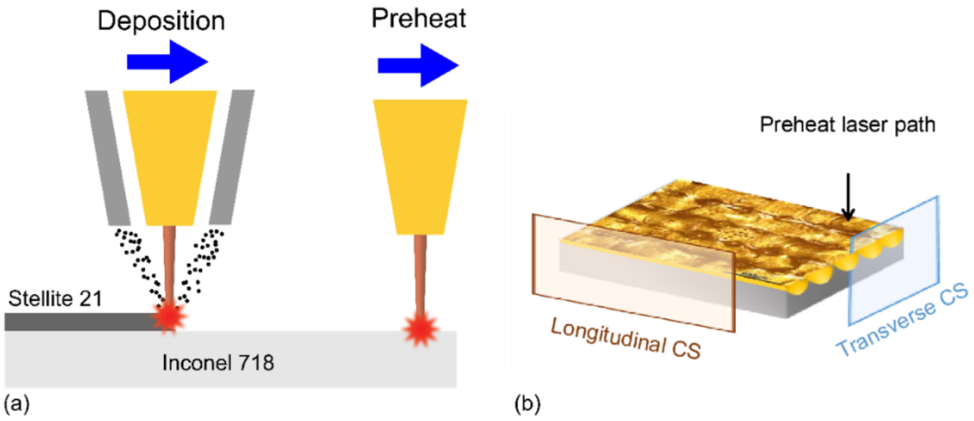

Figure 2: (a) schematic of the preheat and Stellite 21 coating deposition steps, and (b) the cross-sectional planes with respect to the preheat laser path on Inconel 718 prior to the deposition of Stellite 21 coating. The transverse cross-section was made normal to the preheat laser path, exposing peaks and troughs created by preheating.

2.2 Ultrasound Measurements

2.2.1 Experimental Setup

A schematic of the experimental setup used for the ultrasound measurements is shown in Figure 3. Ultrasound measurements were performed using a pulse-echo mode with three different spherically focused broadband immersion transducers. The nominal center frequencies of the transducers were 7.5, 10, and 15 MHz each with a focal length in water, *F*, of 76.2 mm. A computer controlled pulser/ receiver (JSR Ultrasonic model DPR300) was used, and the digitization of the signals used a 100 MHz digitizer A/D AL×GT card (Acquisition Logic). A desktop computer with UTWin interface (Mistras) controlled the data acquisition as well as the transducer motion.

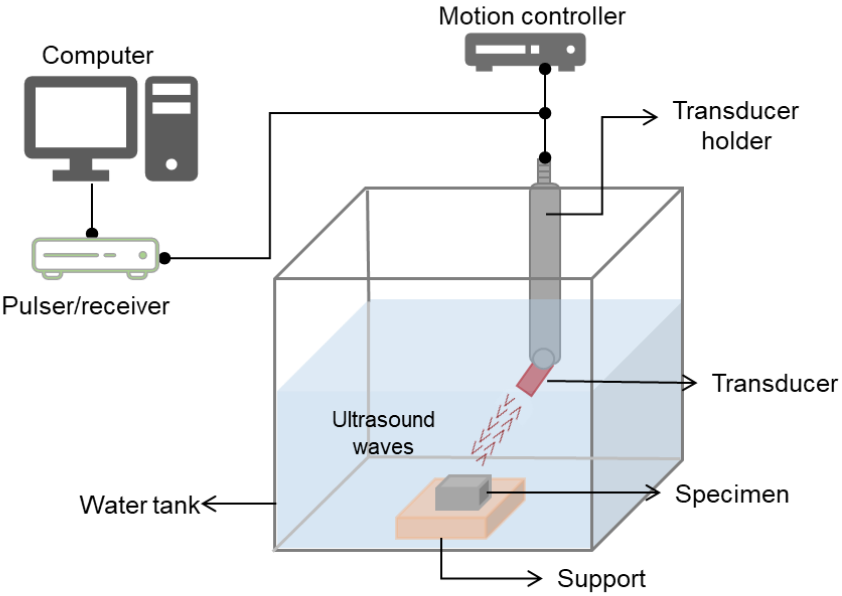

Figure 3: Schematic of the experimental setup for acquiring surface wave measurements.

2.2.2 Calculations of Theoretical Values for Ultrasound Surface Waves

Off-axis (i.e., oblique incidence) measurements were made with the transducer oriented at an angle relative to the normal of the sample surface. Such off-axis ultrasound measurements are commonly used for near-surface inspection applications [38, 53, 55-57]. This oblique-incidence configuration can excite all types of waves, namely longitudinal, shear, and surface waves. However, only surface wave measurements are considered here.

The angle of incidence for the surface waves is determined using Snell's Law. This relation is given by

$$\frac{\sin(\theta_i)}{c_f} = \frac{\sin(\theta_{rL})}{c_L} = \frac{\sin(\theta_{rT})}{c_T}, \tag{1}$$

where, θ_i is the angle of incidence, c_f is the wave speed in the fluid, θ_{rL} is the reflected angle for a longitudinal wave in the sample, c_L is the longitudinal wave speed in the sample, θ_{rT} is the reflected angle for a shear (transverse) wave in the sample, c_T is the shear wave speed in the sample. When $\theta_{rT} = 90°$ in Eq. (1), the propagation path is restricted to the surface and only surface waves are excited. The corresponding incidence angle θ_i is known as the 2nd critical angle.

The surface wave speed (here, a leaky Rayleigh wave) is slower than the shear wave speed, and is related to the material properties by (assuming a homogeneous, isotropic, linearly elastic material) [36, 58]:

$$c_s = \frac{0.862 + 1.14v}{1 + v} \sqrt{\frac{G}{\rho}}, \tag{2}$$

where, c_s is the surface wave speed, v is the Poisson's ratio, *G* is the shear modulus and ρ is the sample density. The surface wave speeds and estimated 2nd critical angles calculated for both materials used here (Stellite 21 and Inconel 718) are reported in Table 3. We note that these estimates are based on a plane wave assumption but the actual field in the sample becomes more complicated due to the shape of the transducer beam and material heterogeneity. A measurement calibration was used to find the maximum amplitude of the surface wave and to reduce the impact of such assumptions.

Table 3: Theoretical values of the surface wave speeds and the 2^{nd} critical angles based on homogenous theory using Eq. (1) and Eq. (2).

	Inconel 718	Stellite 21
Surface Wave Speed, C_s [mm/µs]	2.8	3.1
2^{nd} Critical Angle, θ_2 [°]	29.5	26.2

In surface wave measurements, a coherent reflection from the top surface is not created. Instead, the first signal (i.e., front noise) includes information about the microstructure and, to some extent, is analogous to the diffuse field in transverse and longitudinal measurements [59]. Although the front noise is incoherent, coherent reflections arise when there is a pronounced impedance mismatch, such as geometry change, pore, or impurity.

Because the surface waves are used when there is an interest in the surface region of the sample, the focus is placed on the surface. Hence, the water path, WP, is the focal length of the transducer (i.e., $WP = F$). Nonetheless, the surface wave is expected to penetrate approximately one wavelength in the sample. Therefore, the penetration depth (D) is dependent on the frequency and is given by [60]

$$D = \frac{2\pi c_s}{f}, \tag{3}$$

where f is the center frequency and c_s is the surface wave speed. The surface wave penetration depths calculated for both Stellite 21 and Inconel 718 at different frequencies are given in Table 4. Referring to Figure 4, only the penetration depth for Stellite 21 is assumed for all samples because the maximum penetration depth of the surface wave does not exceed the heat-affected zone (HAZ) and the microstructure of the HAZ is similar to that of the Stellite 21 coating [41].

As depicted in Table 4 and Figure 4, the penetration depth of ultrasound surface wave measurements carried out at three frequencies (7.5, 10, and 15 MHz) corresponds to the scale of crack formation (100-300 µm) and warpage (100-600 µm) observed in this work. Consequently, the surface ultrasound measurements herein are dominated by cracking and warpage, with negligible effect of microstructure-level scattering.

Table 4: Estimated frequency-dependent surface wave penetration depth in the samples assuming D is one wavelength.

	Approximate Penetration Depth, D [µm]	
Frequency, f [MHz]	Inconel 718	Stellite 21
7.5	413	360
10	310	280
15	207	186

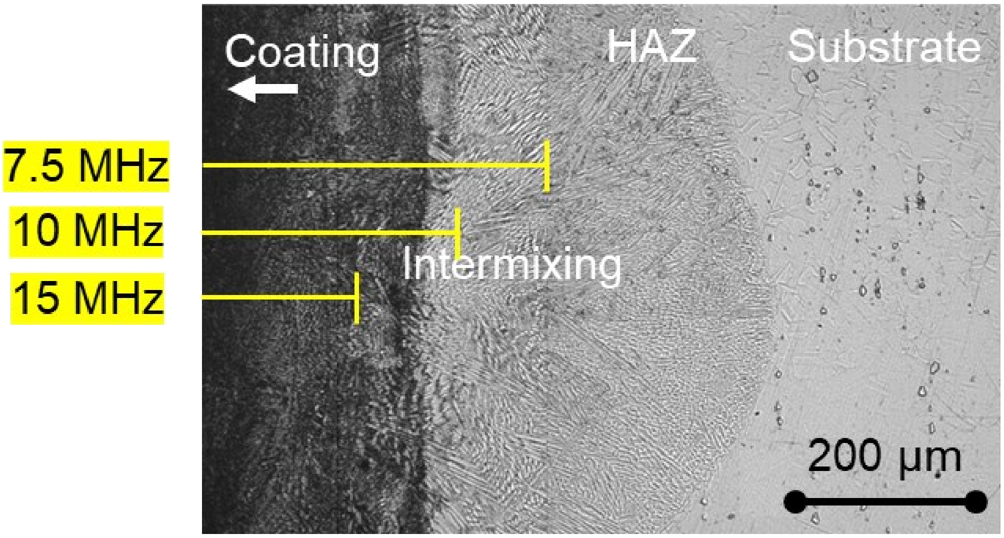

Figure 4: Transverse cross-sectional view of sample N (P_h= 350 W; P_d= 200 W), illustrating the estimated penetration depth of surface waves (approximately one wavelength) at different frequencies.

2.2.3 Calibration and Data Acquisition

A calibration was performed to find the optimal angle of incidence for ultrasonic scanning at each frequency (7.5, 10, and 15 MHz). The water path was selected at the focal length of the transducer in water, 76.2 mm. The transducer was placed such that the reflection from the transverse edge was clearly visible and the distance d to the edge was fixed as shown schematically in Figure 5(a). Then, the transducer was rotated through angles of incidence between 24-37° (based on the theoretical 2nd critical angle) at increments of 0.5°. The incidence angle θ_i, which resulted in the maximum reflected amplitude from the edge, was considered the optimal angle for that specific frequency and used in subsequent experiments. Similarly, optimal angles of incidence were found for Inconel 718 at each frequency for comparison purposes. The values of the optimal angles calibrated for measurements at each frequency are summarized in Table 5

Each surface scan encompassed an area of approximately 10 mm × 10 mm with a step size of 0.25 mm; ~1000 data points were acquired per scan. Figure 5 exemplifies the experimental configuration of the surface wave measurements. For each frequency, a spherically focused transducer was used as depicted in Figure 5(a). The focus of the transducer was placed approximately on the coating surface while the transducer was oriented from the normal to the surface by the corresponding 2nd critical angle for each frequency. For each scan, the transducer translates in the XY plane while transmitting and receiving ultrasonic pulses. An example ultrasonic signal, called an A-scan, is shown in Figure 5(b). A relevant time window is defined by choosing an appropriate gate, as denoted by the red line in Figure 5(b). The gated amplitude from all signals are recorded as a C-scan as shown in Figure 5(c). In this case, the C-scan provided information in terms of the amplitudes of the reflected waveforms inside the predefined time gate; C-scans of the coating surface at each of the three frequencies were collected for all samples. Similarly, a C-scan was performed on an Inconel 718 coupon (substrate). In all cases, the signal window was defined such that the entire grain noise and edge reflection were collected.

To obtain the surface wave speed, the change in arrival time of the edge reflection for consecutive scan signals, Δt, was calculated using a cross-correlation function. Subsequently, the surface wave speed c_S was calculated as $c_s = h/\Delta t$, where h is the step size between measurement positions. To quantify the grain noise in the Stellite coating, the surface wave-diffuse ultrasonic backscatter (SW-DUB) amplitude from each sample was defined as the spatial variance of the backscattered signals and calculated as [61]

$$\Phi(t) = \frac{1}{N}\sum_{i=1}^{N} V_i^2(t) - \left[\frac{1}{N}\sum_{i=1}^{N} V_i(t)\right]^2 , \tag{4}$$

where $V_i(t)$ denotes a single signal at position i. The SW-DUB amplitudes were normalized using the maximum voltage at normal incidence, V_{max}, as $\Phi(t)/V_{max}^2$ [62]. Then, the normalized SW-DUB curve for each condition was fit using a Gaussian [Figure 5(d)], and its maximum was evaluated as a function of preheat and deposition conditions.

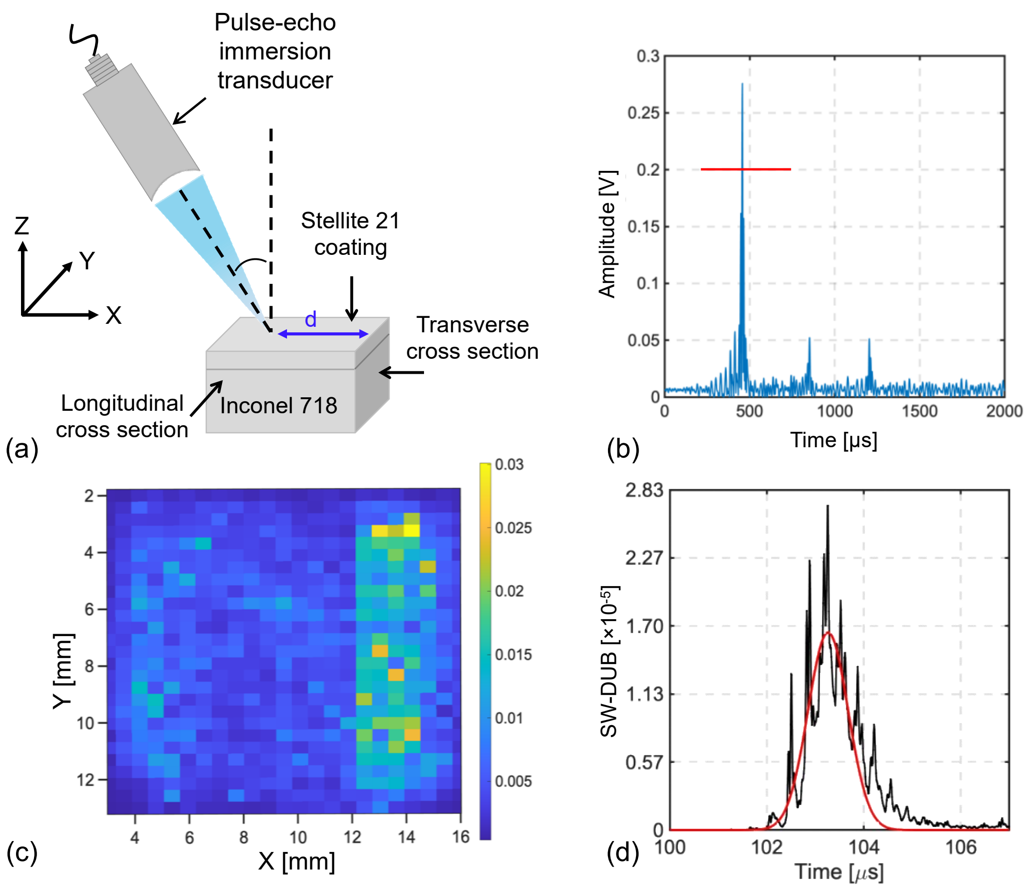

Figure 5: Experimental configuration of ultrasonic surface wave measurements: (a) schematic representation of surface wave measurement system, where θ is the incident angle and d is the distance from the edge, (b) a single waveform (A-scan); the red line denotes the gate used for identifying the area of interest, (c) represents a C-scan of amplitudes within the gate of all A-scans performed on the coating surface (10 mm × 10 mm), and (d) surface wave-diffuse ultrasonic backscatter (SW-DUB) signals, normalized by the square of the maximum voltage at normal incidence, V_{max}, and fit with a Gaussian. The maximum of the Gaussian is used as a metric of the scattering from the sample microstructure.

Table 5: Summary of optimal angles selected based on calibration measurements.

Frequency [MHz]	Optimal Incidence Angle, θ_i [º]	
	Inconel 718	Stellite 21
7.5	33	32.5
10	31.5	34
15	30.5	33

3 Results and discussion

3.1 Microstructure

From Figure 6, we observe that the number of cracks increases significantly with deposition laser power (P_d), regardless of whether the substrate was preheated. For example, samples deposited at a relatively high laser power (P_d= 275W), such as samples F (P_h=0 W) and O (P_h=400 W), have the highest number of cracks and the penetration depth of cracks could reach up to 350 µm. A comparison of the preheated samples, such as sample Q (P_h=400 W; P_d=225 W) and O (P_h=400 W; P_d=275 W), with the corresponding non-preheated samples, P (P_h=0 W; P_d=225 W) and F (P_h=0 W; P_d=275 W), respectively, shows that the cracking was mitigated by preheating the substrate and reducing the deposition laser power.

Occurrence of cracking at a relatively high laser power is attributed to a build up of high thermal-induced residual stresses at the surface due to rapid melting and solidification of the meltpool [41]. Exposing the build to high laser power facilitates diffusion of relatively brittle carbide forming elements, such as Cr, from the dendritic regions into inter-dendritic regions, which in turn increases the propensity of the inter-dendritic region to cracking under high thermal-induced residual stresses [41]. Preheating the substrate decreases steep thermal gradients during the deposition process, and consequently mitigates the thermal-induced residual stresses [41].

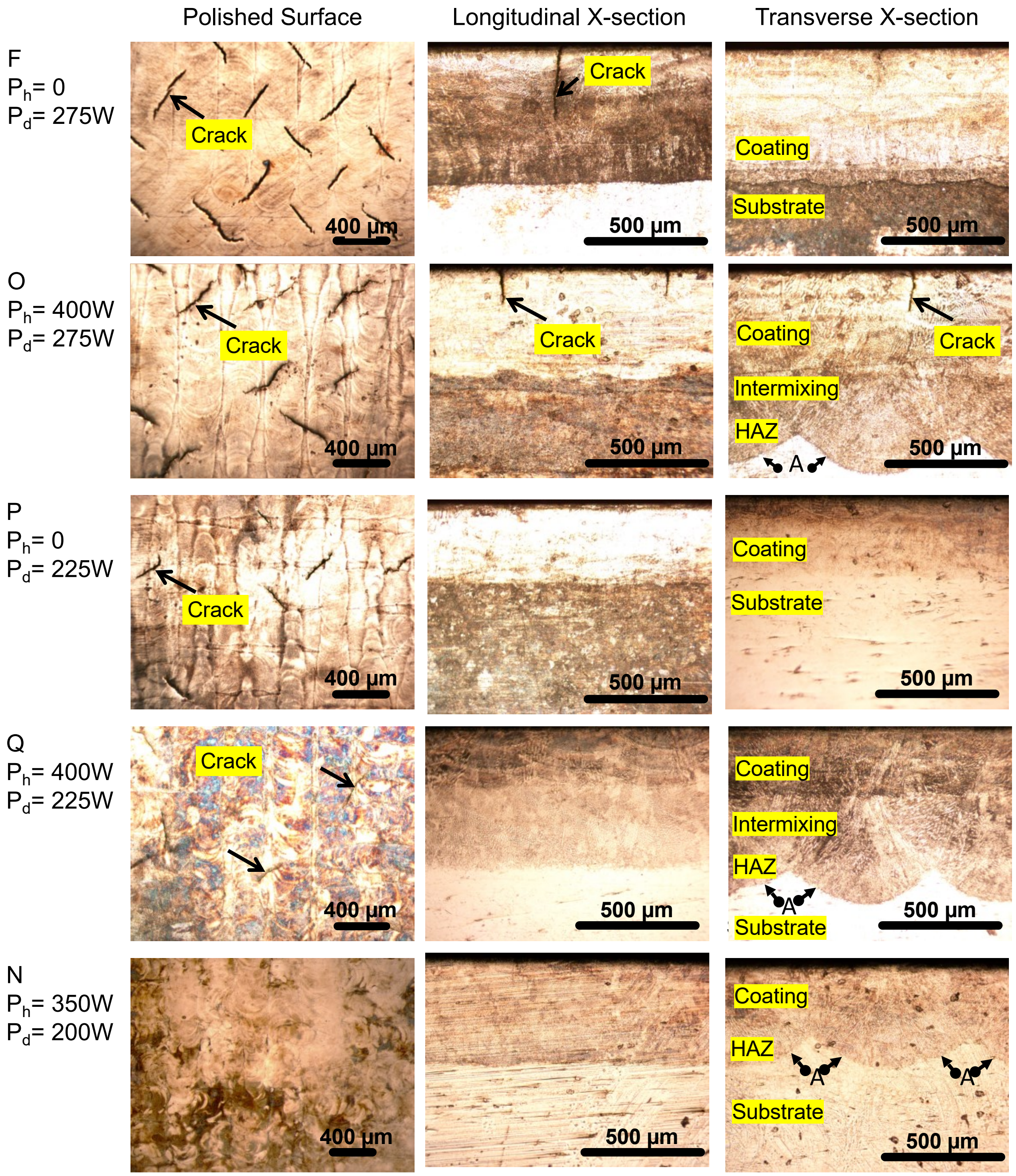

Figure 6: Optical micrographs of the polished and etched surfaces and cross sections of Stellite 21 coating deposited under different preheat and deposition power settings. In samples F and O, which were deposited at a high laser power (P_d = 275W), the surface is replete with cracks. Those cracks are restricted to the top surface and do not extend to the substrate. The maximum depth of an observed crack was 350 µm (sample F). Preheating tends to reduce cracking, as evident from sample P and Q. Preheating also tends to melt the substrate. The presence of troughs and peaks, demarcated as A, indicates that the substrate material was melted during preheating. (Reprinted with permission from Ref. [41]. Copyright 2021, Elsevier).

It is evident from the transverse sections shown in Fig. 6 that the samples with substrate preheating (O, Q, and N) have peaks and troughs corresponding to the laser passes. These geometric features, denoted by *A* in Figure 6, indicate that the substrate material melted and resolidified during preheating (i.e., the local temperature exceeded the solidus temperature of Inconel 718 [1260ºC]). Moreover, samples which were deposited without preheating but at high laser powers, such as sample F, also have peaks and troughs. However, the depth of resolidified substrate material in sample F was in the range of 50 µm, which is much shallower than that of sample O (~200µm). We note that 12 layers of Stellite 21 were deposited. The intended layer thickness in this work was 0.25 mm to produce a total coating thickness of 3 mm. However, the final coating thickness is dependent on the material, the focal plane location with respect to the previous layer, and the process parameters chosen [1, 63, 64]. Thus, the total coating thickness obtained here was 500-600 µm as shown from the transverse views in Figure 6

More importantly, cracks are confined to the topmost layers. This observation is evident in both longitudinal and transverse cross sections in Figure 6 in which no crack is found to exceed 350 µm. To further investigate this observation, the crack penetration depth in a representative coating sample (sample F) was analyzed using X-ray computed tomography (XCT). The XCT results shown in Figure 7 confirm that the crack density decreases with the penetration depth. Additionally, no cracks were observed near the interface, indicating a strong adhesion between the coating and substrate. The presence of cracks confined to the topmost layers is associated with the remelting of the previously deposited layers by subsequent layers [41, 65]. In other words, during the deposition process, the cracks are initiated from the surface of the layer being deposited towards the substrate. The deposition of subsequent layers on the top remelts the previously deposited layers which eliminates the cracks.

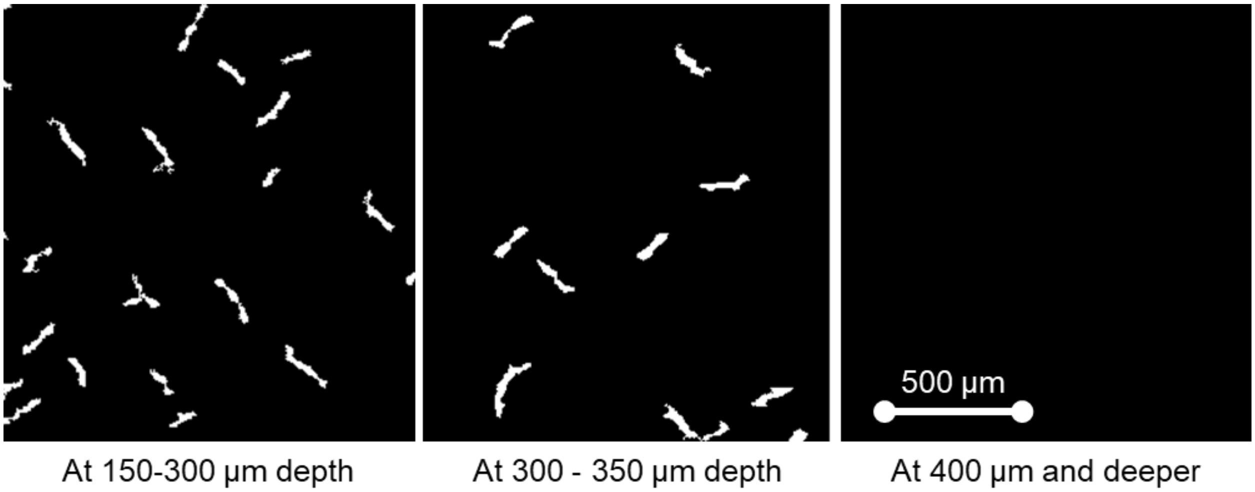

Figure 7: The XCT analysis of crack density along the depth of Stellite 21 coating for a representative sample (Sample F, P_h= 0 W, P_d= 275W). Crack density reduces with the depth from the coating surface. No cracks are found beyond 400 µm depth [41].

Figure 8 shows high resolution SEM images of the polished and etched coating surfaces. The microstructure formed under different processing conditions has a dendritic structure, typical of AM processed materials as a result of high cooling rates. From Figure 8, we observe that the average microstructural features (i.e., grain diameter) represented by the dendritic and inter-dendritic regions is in the range of 3-5 µm. However, the average length and penetration depth of cracking observed on the surface and cross section, as shown in Figure 6, reached several hundred micrometers. An SEM image of a typical crack observed on the coating surface is shown in Figure 8(f). From the SEM investigation, we observed that cracking occurred without exception along the inter-dendritic regions for all cracked coating samples. In addition, it should be noted that the coating microstructure is much smaller than the surface wavelength for even the highest frequency (15 MHz). Thus, the SW-DUB is expected to be dominated by the cracks which are closer in size to the wavelengths used.

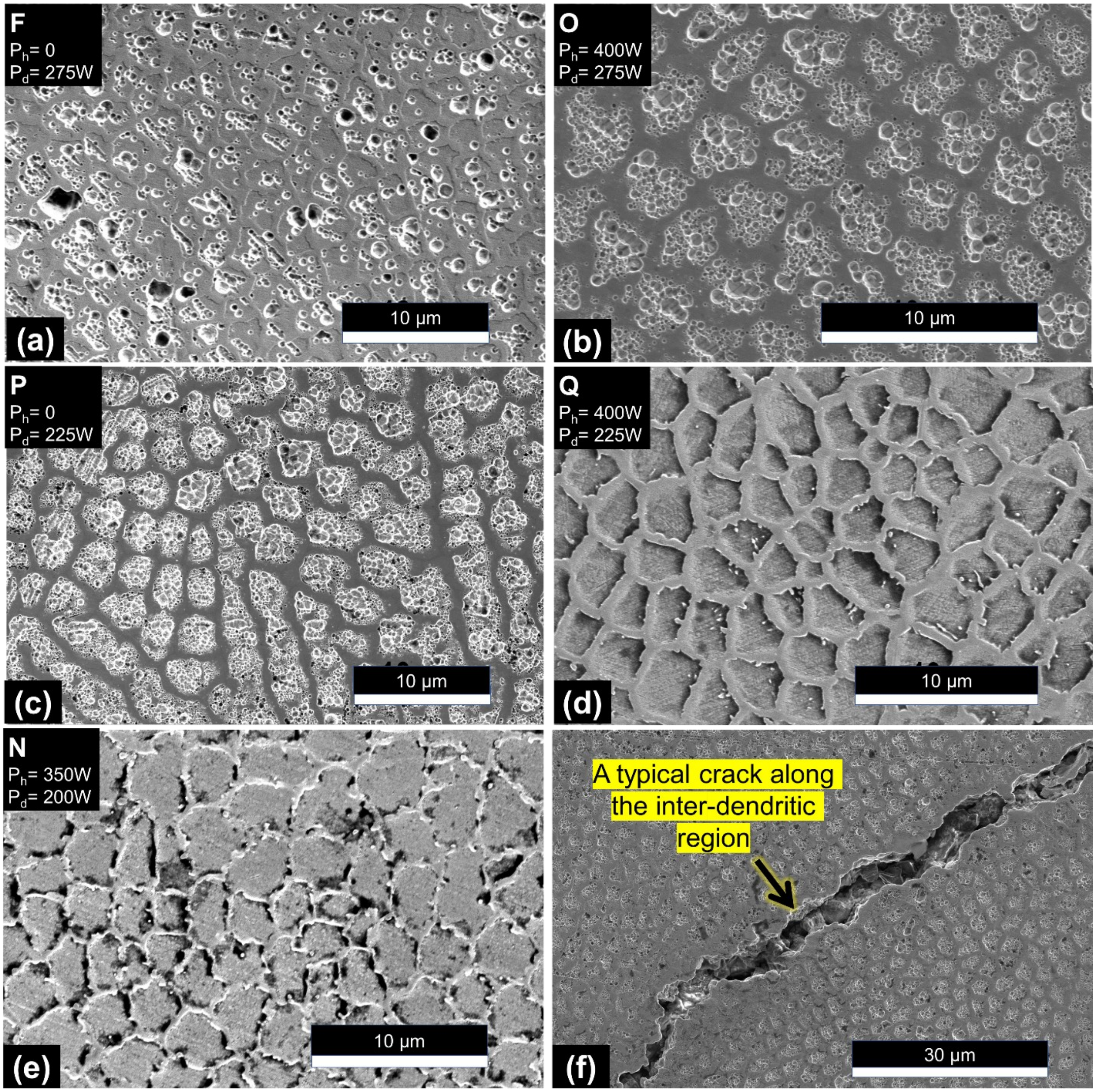

Figure 8: (a-e) SEM images of the polished and etched coating surfaces resulting from different processing conditions. The average size of a microstructural feature represented by dendritic regions ranges from 3-5 µm, while a crack length exceeds several hundred µm and occurs without exception along the inter-dendritic regions. (f) is an SEM image of a typical crack observed on the coating surface.

In Figure 4, which shows high magnification optical micrographs of the transverse cross section of sample N, four different regions can be clearly discerned: surface coating, intermixing, heat affected zone (HAZ), and the substrate material. Surface coating refers to the pure Stellite 21 coating while the intermixing region is the location for which the Stellite coating has been diluted with the elements from the substrate. According to the energy-dispersive X-ray spectroscopy (EDS) results reported in Ref. [41], the width of the intermixing region is proportional to the preheat power. For instance, the highest variation in the concentration of Co, Ni and Cr in samples P (P_h= 0 W), N (P_h= 350 W), and Q (P_h= 400 W) occurred over a distance of ~20, 40, and 200 μm, respectively. In other words, the change in concentration of those elements took place over a longer distance towards the coating surface for the samples deposited with higher preheat.

In the intermixing region, molten materials from both the substrate and deposited coating mix at the interface during the deposition of the first few layers. The intermixing region is larger for preheated samples because the laser melts the substrate surface. The high temperature of the resolidified surface layer thereafter promotes the intermixing of materials during the deposition process. Lastly, the resolidified substrate material, referred to as the heat-affected zone (HAZ), has a dendritic morphology due to the fast cooling rate but maintains the nominal composition of the substrate, without any dilution by the Stellite 21 coating elements. The morphology and EDS elemental analysis of the HAZ are shown in Figure 9(a) and (b), respectively.

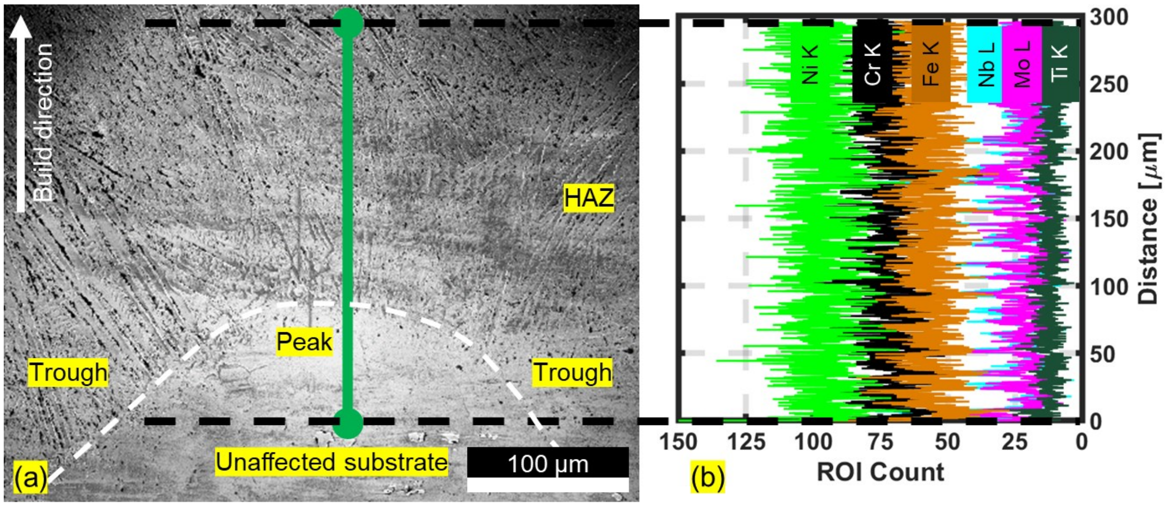

Figure 9: (a) SEM image of the Heat Affected Zone (HAZ) generated by preheating the substrate; (b) Results of EDS line scans performed along the HAZ.

3.2 Crack Density and Sample Warpage

Figure 10 shows the change in crack density and sample warpage for the five samples deposited using different combinations of preheat (P_h) and deposition (P_d) laser powers. To reiterate, samples F and O were deposited at P_d= 275 W, whereas samples P and Q were deposited at P_d= 225 W. Samples F and P were deposited at room temperature without preheat (P_h= 0 W) to serve as control samples for O and Q, respectively, which were deposited after preheating the substrate at P_h= 400 W. in Figure 10 (a), the crack density (η) was determined from SEM images as $\eta = \frac{8}{\pi^3} M l^2$, where M is the total number of cracks per unit area in an SEM image and l is the average length of the cracks [66]. Similar to the results obtained from the optical microscopy (Figure 6), it is observed that lowering the deposition laser power and preheating the substrate reduces crack density as shown in Figure 10 (a). Note that following this trend, crack-free deposition, represented by sample N, was achieved at P_d= 200 W and P_h= 350 W.

Another important observation in DED-processed parts is the tendency to warp due to high residual stresses. In this study, the samples warped in a concave manner. The relative sample warpage was determined as the average of the maximum deviation from the ideal surface plane measured at each edge [41]. The results shown in Figure 10(b) indicate that the preheat laser power (P_h) has the greatest effect on sample warpage. Preheating the substrate at P_h= 400 W resulted in sample warpage of as much as 0.5 mm. Hence, it is necessary to balance the deleterious side-effect of preheating on warpage with the beneficial effect on crack mitigation as represented by sample N.

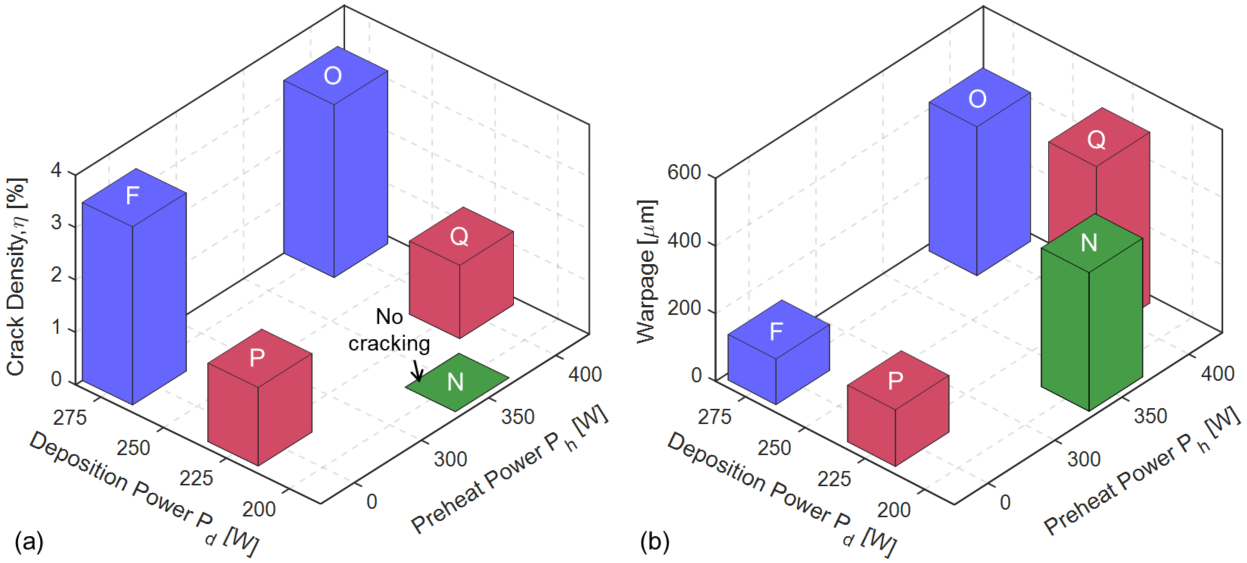

Figure 10: The change in crack density (a), and sample warpage (b) as a function of deposition and preheat laser powers. A significant increase in crack density is observed with increasing the deposition laser power while preheat laser power alleviates cracking. On the other hand, preheated samples show higher warpage as opposed to samples processed without preheat, regardless of deposition laser power.

3.3 Ultrasound Surface Wave Speed Measurements

As shown in Figure 11(a), the measured surface wave speed was below the Stellite 21 theoretical surface wave speed for all the samples. This difference may be explained by the differences in the residual stress state of the samples. Slower wave speeds are expected when tensile residual stresses are present [67, 68]. Thus, higher stresses in a material result in longer wave arrival times than the stress-free material case. While the residual stresses were not measured, the substrate warpage was considered as a surrogate metric to qualify the magnitude of residual stress in the sample. The relationship between warpage and surface wave speed at 7.5 MHz (i.e., the deepest penetration depth) is shown in Figure 11(b). As expected, an inverse relationship is observed. Higher surface wave speed measurements were measured in samples with less warpage; as warpage increased, the surface wave speed decreased. We note that the wavelength of surface wave in this work is comparable to the size of cracks observed (~ 100 µm to 300 µm) and bulk characteristics (warping). Hence, the effect of microstructure-scale aspects on the surface ultrasound measurements specific to the frequencies reported in this work is negligible. Additionally, samples with approximately the same crack density, such as P and Q, exhibited large differences in wave speed. Thus, indicating that residual stress is the dominant factor in the observed wave speed trend.

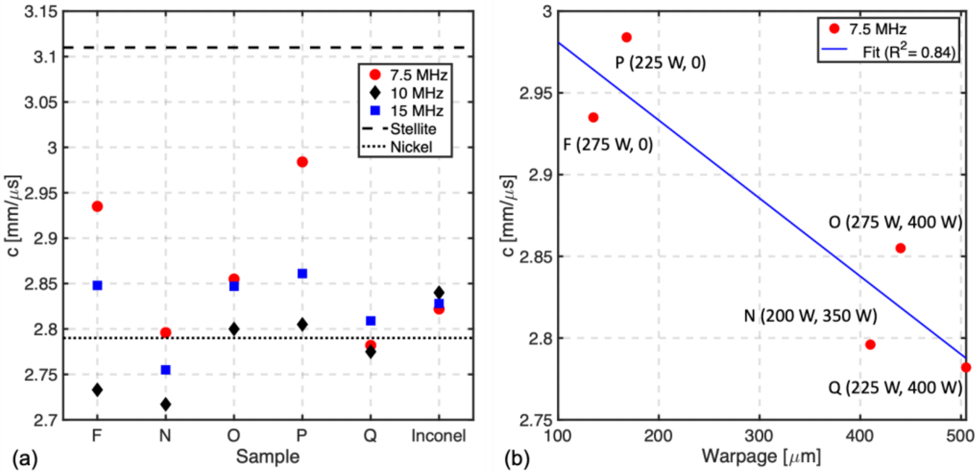

Figure 11: (a) Surface wave speed for all samples at each frequency in comparison with the theoretical values for Stellite 21 and nickel. (b) Surface wave speed vs warpage at 7.5 MHz. Higher substrate warpage results from higher tensile residual stresses and leads to lower surface wave speed.

3.4 Surface Wave Diffuse Ultrasonic Backscatter (SW-DUB)

Figure 12 reports maximum amplitude of the surface wave diffuse ultrasonic backscatter ($\text{SW-DUB}_{\text{max}}$) calculated for all samples including the Inconel 718 substrate at different frequencies. It is observed that $\text{SW-DUB}_{\text{max}}$ changes as a function of preheat and deposition laser power at any given frequency. From Figure 12(a), it can be deduced that $\text{SW-DUB}_{\text{max}}$ is greatly affected by the preheat condition when a relatively low frequency is used (7.5 MHz). This outcome is reasonable because, as illustrated in Figure 4, the penetration depth of the surface waves excited at 7.5 MHz should have reached the heat-affected zone (HAZ) of the samples. Hence, the high residual stresses generated in the HAZ with respect to the substrate result in higher $\text{SW-DUB}_{\text{max}}$.

At 10 MHz, shown in Figure 12(b), an increasing trend of $\text{SW-DUB}_{\text{max}}$ with a decrease of the deposition laser power is observed. At this frequency, the penetration depth of the surface waves in Stellite 21 reaches the intermixing region, in which the coating dilution with the substrate material increases with the deposition laser power and preheating the substrate [41]. In other words, the $\text{SW-DUB}_{\text{max}}$ signals at 10 MHz are affected by both the preheat and deposition conditions; and it is higher for the samples with smaller intermixing regions.

Although preheating the substrate increases the intermixing between the coating and substrate, it nonetheless reduces the strong thermal stresses that accompany the coating deposition at room temperature [69]. However, preheating the substrate also generates some residual stresses in the HAZ with respect to the substrate and it serves as one of the multiple macrostructural factors that balance the effect of the relatively higher intermixing region for preheated samples. Accordingly, the $\text{SW-DUB}_{\text{max}}$ signals at 10 MHz are higher for samples deposited at low deposition power but high preheat power.

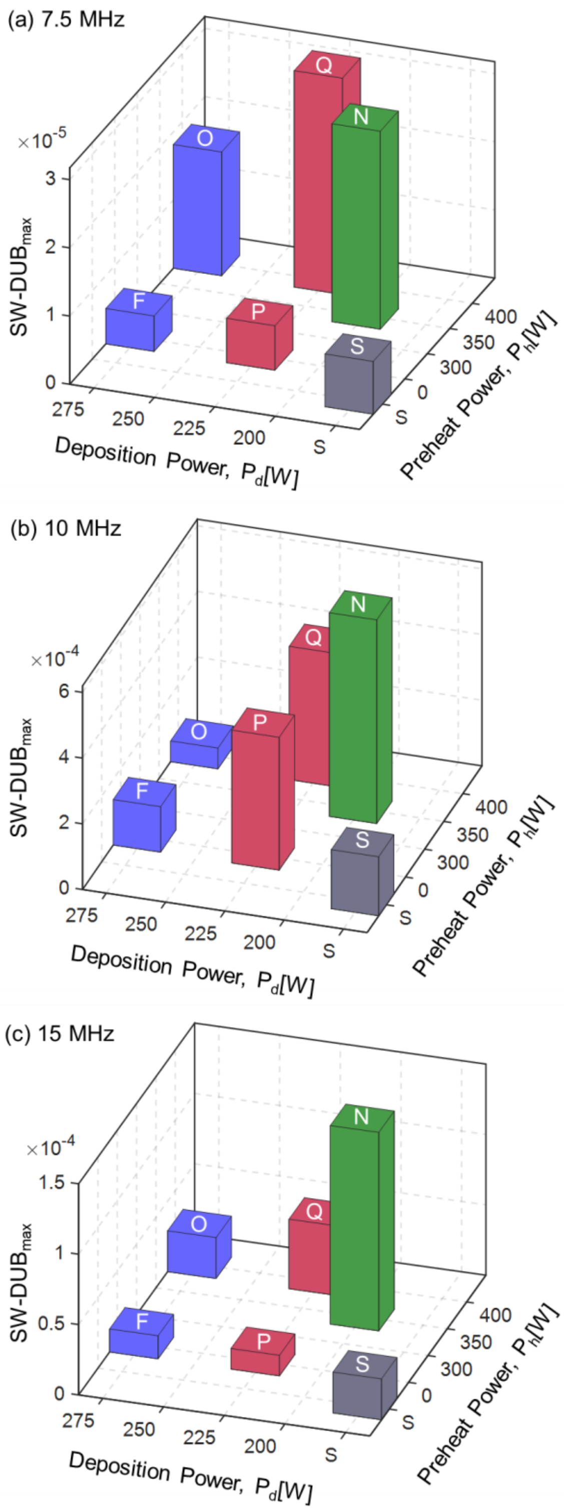

Figure 12: Graphical representation of the surface wave diffuse ultrasound backscatter maximum amplitude (SW-DUB$_{max}$) for all samples at different frequencies: (a) 7.5 MHz, (b) 10 MHz, and (c) 15 MHz The Inconel 718 substrate (S) has the coordinates (s, s) for comparison purposes.

Figure 12(c) reveals that the SW-DUB$_{max}$ behavior at 15 MHz is affected by the preheating condition of the samples and consequently the stress state of the coating. The samples with low crack density resulted in higher SW-DUB$_{max}$. Because the penetration depth of surface waves at 15 MHz is confined mostly to the coating, the surface wave scattering is more affected by the stress state of the coating. In our previous work, Ref. [41], it was shown that the brittle, inter-dendritic cracking of the Stellite 21 coating on Inconel 718 resulted from high thermal stresses that developed during the deposition process.

In other words, cracking relieved the stress state of these samples. Hence, samples with high crack density, such as F, O, and P, shown in Figure 6, have the lowest buildup of residual stresses and consequently the lowest SW-DUB$_{max}$. On the other hand, the crack-free sample N resulted in the highest SW-DUB$_{max}$ due to the retained stress state of the coating. These observations suggest that the SW-DUB$_{max}$ amplitude decreases with crack density due to two factors: the change in the stress state due to cracking, and the crack orientation (~45°) with respect to the direction of surface wave propagation. This observation is corroborated in the work of Hauck *et. al.* [57], who report a similar phenomenon wherein the surface wave amplitude decreases with crack density.

To analyze the effects from residual stress namely, crack density and warpage, on the SW-DUB signals, the relationship between them at 10 MHz is plotted in Figure 13. A prominent inverse linear relationship ($R^2 \sim 98\%$) is observed between the crack density and SW-DUB$_{max}$ at 10 MHz, as shown in Figure 13(a). A similar trend is observed at 7.5 MHz and 15 MHz; however, the linear correlation is less pronounced.

The effect of sample warpage on SW-DUB$_{max}$ signals was also investigated at the three frequencies and a clear relationship was observed only at 7.5 MHz as shown in Figure 13(b). SW-DUB$_{max}$ is more sensitive to the lowest frequency (7.5 MHz) because the penetration depth of the ultrasound wave is higher and reaches the intermixing region. The increase in SW-DUB$_{max}$, in this case, is attributed to the residual stresses that were induced to the substrate due to preheating.

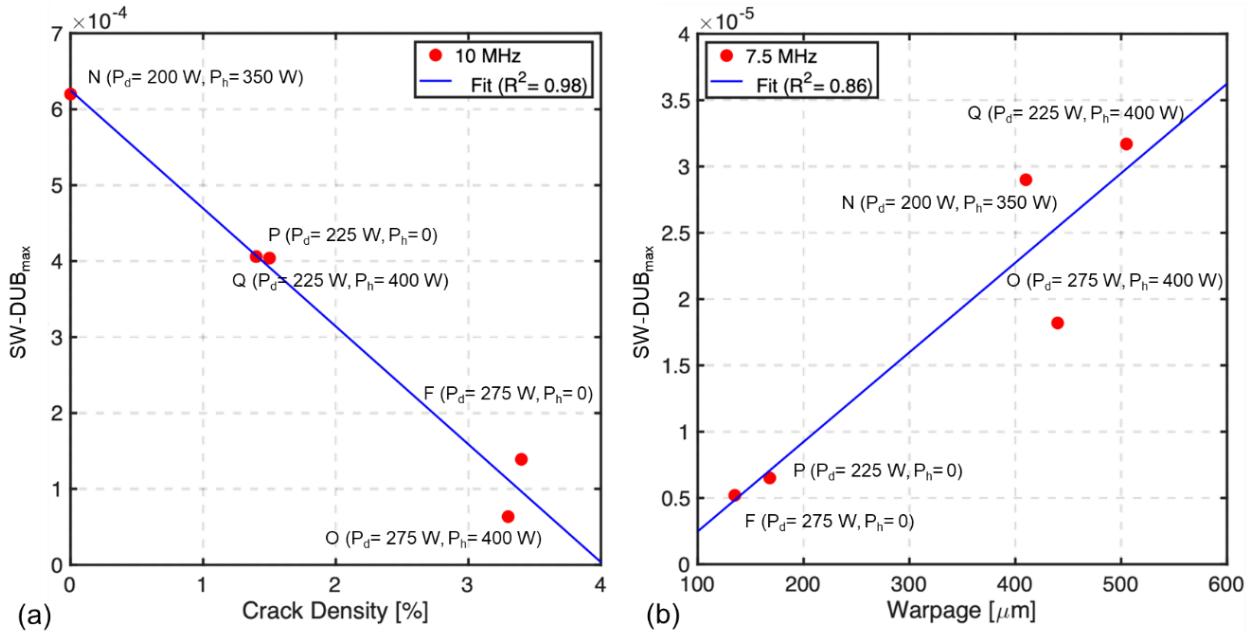

Figure 13: (a) Relationship between the crack density and the maximum amplitude of the surface wave diffuse ultrasound backscatter (SW-DUB$_{max}$) at 10MHz. Cracking relieves residual stresses in the coating, leading to lower SW-DUB$_{max}$. (b) Relationship between SW-DUB$_{max}$ signals and sample warpage due to preheating of the substrate. Preheated samples yield a higher SW-DUB$_{max}$ at 7.5 MHz

4 Conclusion

In this article, ultrasound surface waves were used to evaluate the quality (cracking and warpage) of DED-processed Stellite 21 coatings on Inconel 718 under different preheat and deposition laser powers. Specifically, we observed that the backscatter behavior of ultrasound surface waves was related to the crack density and processing conditions (laser power, and preheat), which in turn influenced the microstructure evolution. The ultrasound frequency controls the penetration depth of the surface waves within the sample, such that the smallest frequency (7.5 MHz) had the highest penetration depth. Thus, several conclusions can be made.

The signals obtained from the measurements at the three frequencies (7.5, 10, and 15 MHz) studied, encapsulated the state of the surface coating, intermixing, and the heat-affected zone (HAZ). Thus, future studies of different coating-substrate combinations can be designed with these outcomes in mind. Under certain processing conditions, thermal stresses were generated in the Stellite 21 coating that led to cracking.

Although such cracks should increase the scattering of surface waves, they also relieve the residual stresses of the sample and lower the surface wave diffuse ultrasonic backscatter (SW-DUB) amplitude. This effect was more pronounced at 15 MHz.

The thickness of the intermixing region was captured at 10 MHz; a thinner intermixing region results in a higher SW-DUB amplitude. This outcome is associated with the different scattering properties of the coating-intermixing-substrate region. The surface wave interacts with a sharper transition from Stellite 21 to Inconel 718, which produces higher scattering due to the impedance mismatch.

The severity of sample warping was captured when a low frequency of 7.5 MHz was used in both SW-DUB amplitude and the surface wave speed. The sample warpage was caused by the residual stresses generated from preheating the substrate and such stresses are known to change wave speed and scattering. Such information can be used for the design of future experiments with a focus on residual stress. Overall, this work demonstrates the potential for nondestructive ultrasound surface waves to evaluate DED-processed coatings and thereupon minimize the need for destructive evaluation.

Acknowledgements

Prahalada Rao thanks the National Science Foundation (NSF) and Department of Energy (DoE) for funding his work under awards OIA-1929172, CMMI-1920245, CMMI-1739696, ECCS-2020246, PFI-TT 2044710, CMMI-1752069, CMMI-1719388, and DE-SC0021136. Understanding the causal influence of process parameters on part quality and detection of defect formation was the major aspect of CMMI-1752069 (Program Officer: Kevin Chou). Supplemental funding for CMMI-1752069 was obtained through the NSF INTERN program (Program Officer: Prakash Balan) and CMMI Data Science Activities (Program Officer: Martha Dodson) is greatly appreciated. The later supplement funded Ziyad Smoqi and Aniruddha Gaikwad's research. The materials characterization research was performed in part in the Nebraska Nanoscale Facility: National Nanotechnology Coordinated Infrastructure under award no. ECCS: 2025298, and with support from the Nebraska Research Initiative through the Nebraska Center for Materials and Nanoscience and the Nanoengineering Research Core Facility at the University of Nebraska-Lincoln.

References

[1] I. Gibson, D.W. Rosen, B. Stucker, Additive manufacturing technologies, Springer2014.

[2] N.A. Kistler, D.J. Corbin, A.R. Nassar, E.W. Reutzel, A.M. Beese, Effect of processing conditions on the microstructure, porosity, and mechanical properties of Ti-6Al-4V repair fabricated by directed energy deposition, Journal of Materials Processing Technology 264 (2019) 172-181. https://doi.org/10.1016/j.jmatprotec.2018.08.041

[3] Y.P. Kathuria, Some aspects of laser surface cladding in the turbine industry, Surface and Coatings Technology 132(2) (2000) 262-269. https://doi.org/10.1016/S0257-8972(00)00735-0

[4] D. Svetlizky, M. Das, B. Zheng, A.L. Vyatskikh, S. Bose, A. Bandyopadhyay, J.M. Schoenung, E.J. Lavernia, N. Eliaz, Directed energy deposition (DED) additive manufacturing: Physical characteristics, defects, challenges and applications, Materials Today 49 (2021) 271-295. https://doi.org/10.1016/j.mattod.2021.03.020

[5] H. Taheri, M. Shoaib, L.W. Koester, T.A. Bigelow, P.C. Collins, L.J. Bond, Powder-based additive manufacturing - a review of types of defects, generation mechanisms, detection, property evaluation and metrology, (2017). https://doi.org/10.1504/IJASMM.2017.088204

[6] Z. Smoqi, B.D. Bevans, A. Gaikwad, J. Craig, A. Abul-Haj, B. Roeder, B. Macy, J.E. Shield, P. Rao, Closed-loop control of meltpool temperature in directed energy deposition, Materials & Design 215 (2022) 110508. https://doi.org/10.1016/j.matdes.2022.110508

[7] A. Ramalho, T.G. Santos, B. Bevans, Z. Smoqi, P. Rao, J.P. Oliveira, Effect of contaminations on the acoustic emissions during wire and arc additive manufacturing of 316L stainless steel, Additive Manufacturing 51 (2022) 102585. https://doi.org/10.1016/j.addma.2021.102585

[8] W.C. Ke, J.P. Oliveira, B.Q. Cong, S.S. Ao, Z.W. Qi, B. Peng, Z. Zeng, Multi-layer deposition mechanism in ultra high-frequency pulsed wire arc additive manufacturing (WAAM) of NiTi shape memory alloys, Additive Manufacturing 50 (2022) 102513. https://doi.org/10.1016/j.addma.2021.102513

[9] T.A. Rodrigues, J.D. Escobar, J. Shen, V.R. Duarte, G.G. Ribamar, J.A. Avila, E. Maawad, N. Schell, T.G. Santos, J.P. Oliveira, Effect of heat treatments on 316 stainless steel parts fabricated by wire and arc additive manufacturing : Microstructure and synchrotron X-ray diffraction analysis, Additive Manufacturing 48 (2021) 102428. https://doi.org/10.1016/j.addma.2021.102428

[10] M.C. Brennan, J.S. Keist, T.A. Palmer, Defects in Metal Additive Manufacturing Processes, Journal of Materials Engineering and Performance 30(7) (2021) 4808-4818. https://doi.org/10.1007/s11665-021-05919-6

[11] L.D. Sotelo, R. Karunakaran, C.S. Pratt, M.P. Sealy, J.A. Turner, Ultrasound in situ characterization of hybrid additively manufactured Ti6Al4V, The Journal of the Acoustical Society of America 150(6) (2021) 4452-4463. https://doi.org/10.1121/10.0008972

[12] Z. Smoqi, A. Gaikwad, B. Bevans, M.H. Kobir, J. Craig, A. Abul-Haj, A. Peralta, P. Rao, Monitoring and Prediction of Porosity in Laser Powder Bed Fusion using Physics-informed Meltpool

Signatures and Machine Learning, Journal of Materials Processing Technology (2022) 117550. https://doi.org/10.1016/j.jmatprotec.2022.117550

[13] L.D. Sotelo, H. Hadidi, C.S. Pratt, M.P. Sealy, J.A. Turner, Ultrasonic mapping of hybrid additively manufactured 420 stainless steel, Ultrasonics 110 (2021) 106269. https://doi.org/10.1016/j.ultras.2020.106269

[14] A. Lopez, R. Bacelar, I. Pires, T.G. Santos, J.P. Sousa, L. Quintino, Non-destructive testing application of radiography and ultrasound for wire and arc additive manufacturing, Additive Manufacturing 21 (2018) 298-306. https://doi.org/10.1016/j.addma.2018.03.020

[15] F. Honarvar, A. Varvani-Farahani, A review of ultrasonic testing applications in additive manufacturing: Defect evaluation, material characterization, and process control, Ultrasonics 108 (2020) 106227. https://doi.org/10.1016/j.ultras.2020.106227

[16] A.A. Hassen, M.M. Kirka, Additive Manufacturing: The rise of a technology and the need for quality control and inspection techniques, Materials Evaluation 76(4) (2018) 438-453.

[17] N. Huang, O.J. Cook, R.L.W. Smithson, C.M. Kube, A.P. Argüelles, A.M. Beese, Use of ultrasound to identify microstructure-property relationships in 316 stainless steel fabricated with binder jet additive manufacturing, Additive Manufacturing 51 (2022) 102591. https://doi.org/10.1016/j.addma.2021.102591

[18] H. Rieder, A. Dillhöfer, M. Spies, J. Bamberg, T. Hess, Online monitoring of additive manufacturing processes using ultrasound, Proceedings of the 11th European Conference on Non-destructive testing 1 (2014) 2194-2201.

[19] H.M. Ledbetter, N.V. Frederick, M.W. Austin, Elastic-constant variability in stainless-steel 304, Journal of Applied Physics 51(1) (1980) 305-309. https://doi.org/10.1063/1.327371

[20] R.J. Smith, W. Li, J. Coulson, M. Clark, M.G. Somekh, S.D. Sharples, Spatially resolved acoustic spectroscopy for rapid imaging of material microstructure and grain orientation, Meas. Sci. Technol. 25(5) (2014) 055902. https://doi.org/10.1088/0957-0233/25/5/055902

[21] A. Wydra, A.M. Chertov, R.G. Maev, C.M. Kube, H. Du, J.A. Turner, Grain size measurement of copper spot welding caps via ultrasonic attenuation and scattering experiments, Research in Nondestructive Evaluation 26(4) (2015) 225-243. https://doi.org/10.1080/09349847.2015.1038407

[22] W.P. Mason, H. McSkimin, Attenuation and scattering of high frequency sound waves in metals and glasses, The Journal of the Acoustical Society of America 19(3) (1947) 464-473. https://doi.org/10.1121/1.1916504

[23] R.L. Weaver, Diffusivity of ultrasound in polycrystals, Journal of the Mechanics and Physics of Solids 38(1) (1990) 55-86. https://doi.org/10.1016/0022-5096(90)90021-U

[24] R.B. Thompson, F.J. Margetan, P. Haldipur, L. Yu, A. Li, P. Panetta, H. Wasan, Scattering of elastic waves in simple and complex polycrystals, Wave Motion 45(5) (2008) 655-674. https://doi.org/10.1016/j.wavemoti.2007.09.008

[25] T.V. da Cunha, C.E.N. Bohórquez, Ultrasound in arc welding: A review, Ultrasonics 56 (2015) 201-209. https://doi.org/10.1016/j.ultras.2014.10.007

[26] B. Chassignole, R. El Guerjouma, M.A. Ploix, T. Fouquet, Ultrasonic and structural characterization of anisotropic austenitic stainless steel welds: Towards a higher reliability in ultrasonic non-destructive testing, NDT & E International 43(4) (2010) 273-282. https://doi.org/10.1016/j.ndteint.2009.12.005

[27] D. Shahriari, A. Zolfaghari, F. Masoumi, Determination of Flaw Type and Location Using an Expert Module in Ultrasonic Nondestructive Testing for Weld Inspection, AIP Conference Proceedings 1315(1) (2011) 825-830. https://doi.org/10.1063/1.3552553

[28] M. Tabatabaeipour, J. Hettler, S. Delrue, K. Van Den Abeele, Non-destructive ultrasonic examination of root defects in friction stir welded butt-joints, NDT & E International 80 (2016) 23-34. https://doi.org/10.1016/j.ndteint.2016.02.007

[29] H. Taheri, M. Kilpatrick, M. Norvalls, W.J. Harper, L.W. Koester, T. Bigelow, L.J. Bond, Investigation of Nondestructive Testing Methods for Friction Stir Welding, Metals 9(6) (2019) 624. https://doi.org/10.3390/met9060624

[30] M.A. Machado, P.L. Inácio, R.A. Santos, A.F. Gomes, A.P. Martins, M.S. Carvalho, T.G. Santos, Inspection of composite parts produced by additive manufacturing: air-coupled ultrasound and thermography, 58th Annual British Conference on Non-Destructive Testing. Telford, UK (2019).

[31] S. Zamen, E. Dehghan-Niri, H. Al-Beer, J. Lindahl, A.A. Hassen, Characterization of nonlinear ultrasonic waves behavior while interacting with poor interlayer bonds in large-scale additive manufactured materials, NDT & E International 127 (2022) 102602. https://doi.org/10.1016/j.ndteint.2022.102602

[32] E. Bozek, S. McGuigan, Z. Snow, E.W. Reutzel, J. Rivière, P. Shokouhi, Nonlinear resonance ultrasonic spectroscopy (NRUS) for the quality control of additively manufactured samples, NDT & E International 123 (2021) 102495. https://doi.org/10.1016/j.ndteint.2021.102495

[33] J.A. Slotwinski, E.J. Garboczi, K.M. Hebenstreit, Porosity Measurements and Analysis for Metal Additive Manufacturing Process Control, J. RES. NATL. INST. STAN. 119 (2014) 494. https://doi.org/10.6028/jres.119.019

[34] C. Kim, H. Yin, A. Shmatok, B.C. Prorok, X. Lou, K.H. Matlack, Ultrasonic nondestructive evaluation of laser powder bed fusion 316L stainless steel, Additive Manufacturing 38 (2021) 101800. https://doi.org/10.1016/j.addma.2020.101800

[35] J. Williams, P. Dryburgh, A. Clare, P. Rao, A. Samal, Defect detection and monitoring in metal additive manufactured parts through deep learning of spatially resolved acoustic spectroscopy signals, Smart and Sustainable Manufacturing Systems 2(1) (2018).

[36] K.J. Harke, N. Calta, J. Tringe, D. Stobbe, Laser-based ultrasound interrogation of surface and sub-surface features in advanced manufacturing materials, Scientific Reports 12(1) (2022) 3309. 10.1038/s41598-022-07261-w

[37] W. Xu, J. Zhang, X. Li, S. Yuan, G. Ma, Z. Xue, X. Jing, J. Cao, Intelligent denoise laser ultrasonic imaging for inspection of selective laser melting components with rough surface, NDT & E International 125 (2022) 102548. https://doi.org/10.1016/j.ndteint.2021.102548

[38] C. Bakre, A.R. Nassar, E.W. Reutzel, C.J. Lissenden, Ultrasonic Rayleigh Wave Interrogation of Directed Energy Deposition Ti–6Al–4V Having a Rough Surface, Journal of Nondestructive Evaluation, Diagnostics and Prognostics of Engineering Systems 5(3) (2022). 10.1115/1.4054539

[39] Q.Y. Lu, C.H. Wong, Additive manufacturing process monitoring and control by non-destructive testing techniques: challenges and in-process monitoring, Virtual and Physical Prototyping 13(2) (2018) 39-48. https://doi.org/10.1080/17452759.2017.1351201

[40] S. Yuan, X. Yu, Ultrasonic non-destructive evaluation of selectively laser-sintered polymeric nanocomposites, Polymer Testing 90 (2020) 106705. https://doi.org/10.1016/j.polymertesting.2020.106705

[41] Z. Smoqi, J. Toddy, H. Halliday, J.E. Shield, P. Rao, Process-structure relationship in the directed energy deposition of cobalt-chromium alloy (Stellite 21) coatings, Materials & Design 197 (2021) 109229. https://doi.org/10.1016/j.matdes.2020.109229

[42] A.T. Clare, O. Oyelola, T.E. Abioye, P.K. Farayibi, Laser cladding of rail steel with Co–Cr, Surface Engineering 29(10) (2013) 731-736. https://doi.org/10.1179/1743294412Y.0000000075

[43] J. Foster, C. Cullen, S. Fitzpatrick, G. Payne, L. Hall, J. Marashi, Remanufacture of hot forging tools and dies using laser metal deposition with powder and a hard-facing alloy Stellite 21®, Jnl Remanufactur 9(3) (2019) 189-203. https://doi.org/10.1007/s13243-018-0063-9

[44] M.X. Yao, J.B.C. Wu, Y. Xie, Wear, corrosion and cracking resistance of some W- or Mo-containing Stellite hardfacing alloys, Materials Science and Engineering: A 407(1) (2005) 234-244. https://doi.org/10.1016/j.msea.2005.06.062

[45] H. Shi, J.-R. Cho, D.-G. An, Microstructure and hardness of Stellite 21 deposited on hot forging die using direct metal deposition technology, Journal of Mechanical Science & Technology 34(3) (2020). https://doi.org/10.1007/s12206-020-0227-z

[46] K.C. Antony, Wear-resistant cobalt-base alloys, JOM 35(2) (1983) 52-60. https://doi.org/10.1007/BF03338205

[47] D. Coutsouradis, A. Davin, M. Lamberigts, Cobalt-based superalloys for applications in gas turbines, Materials Science and Engineering 88 (1987) 11-19. https://doi.org/10.1016/0025-5416(87)90061-9

[48] W.S. de Rosset, J.S. Montgomery, Cobalt-base alloy gun barrel study, Wear 316(1) (2014) 119-123. https://doi.org/10.1016/j.wear.2014.05.001

[49] P. Crook, Cobalt and cobalt alloys, ASM International, Metals Handbook, Tenth Edition. 2 (1990) 446-454. https://doi.org/10.31399/asm.hb.v02.a0001073

[50] V.K. Nadimpalli, L. Yang, P.B. Nagy, In-situ interfacial quality assessment of Ultrasonic Additive Manufacturing components using ultrasonic NDE, NDT & E International 93 (2018) 117-130. https://doi.org/10.1016/j.ndteint.2017.10.004

[51] S. Islam, S.P. Deshpande, L.D. Sotelo, M. Norouzian, M.T. Lumpkin, L.F. Ammerlaan, A.J. Fuller, J.A. Turner, Quantitative Ultrasonic Characterization of Subsurface Inclusions in Tapered Roller Bearings, in: J.M. Beswick (Ed.), Bearing Steel Technologies: 12th Volume, Progress in Bearing Steel Metallurgical Testing and Quality Assurance, ASTM International, 100 Barr Harbor Drive, PO Box C700, West Conshohocken, PA 19428-2959, 2020, pp. 66-81.

[52] D. Chen, H. Xiao, J. Xu, An improved Richardson-Lucy iterative algorithm for C-scan image restoration and inclusion size measurement, Ultrasonics 91 (2019) 103-113. https://doi.org/10.1016/j.ultras.2018.07.021

[53] L. Koester, C. Zuhlke, D. Alexander, A. Fuller, B. Wilson, J. Turner, Near-race ultrasonic detection of subsurface defects in bearing rings, Bearing Steel Technologies: 9th Volume, Advances in Rolling Contact Fatigue Strength Testing and Related Substitute Technologies, ASTM International2012.

[54] C. Tarawneh, L. Koester, A. Fuller, B. Wilson, J. Turner, Service Life Testing of Components with Defects in the Rolling Contact Fatigue Zone, Bearing Steel Technologies: 9th Volume, Advances in Rolling Contact Fatigue Strength Testing and Related Substitute Technologies (2012). https://doi.org/10.1520/STP104628

[55] D. Hesse, P. Cawley, Detection of Critical Defects in Rails Using Ultrasonic Surface Waves, AIP Conference Proceedings 894(1) (2007) 1413-1420. https://doi.org/10.1063/1.2718132

[56] G. Fitzpatrick, B. Hildebrand, Near surface flaw detection by ultrasonic critical angle imaging, Journal of Nondestructive Evaluation 3(4) (1982) 201-220. https://doi.org/10.1007/BF00565865

[57] E. Hauck, J.L. Rose, W.-J. Song, D.F. Heaney, A surface wave mediator technique for crack detection in green parts, Advances in Powder Metallurgy and Particulate Materials (9) (2003) 9-154.

[58] B.A. Auld, Acoustic Fields and Waves in Solids, Wiley1973.

[59] P.B. Nagy, J.H. Rose, Surface roughness and the ultrasonic detection of subsurface scatterers, Journal of Applied Physics 73(2) (1993) 566-580. https://doi.org/10.1063/1.353366

[60] J.L. Rose, Ultrasonic Guided Waves in Solid Media, Cambridge University Press2014.

[61] P. Hu, C.M. Kube, L.W. Koester, J.A. Turner, Mode-converted diffuse ultrasonic backscatter, The Journal of the Acoustical Society of America 134(2) (2013) 982-990. https://doi.org/10.1121/1.4812769

[62] G. Ghoshal, J.A. Turner, Diffuse ultrasonic backscatter at normal incidence through a curved interface, The Journal of the Acoustical Society of America 128(6) (2010) 3449-3458. https://doi.org/10.1121/1.3500683

[63] Y. Hu, W. Cong, A review on laser deposition-additive manufacturing of ceramics and ceramic reinforced metal matrix composites, Ceramics International 44(17) (2018) 20599-20612. https://doi.org/10.1016/j.ceramint.2018.08.083

[64] D.-S. Shim, G.-Y. Baek, J.-S. Seo, G.-Y. Shin, K.-P. Kim, K.-Y. Lee, Effect of layer thickness setting on deposition characteristics in direct energy deposition (DED) process, Optics & Laser Technology 86 (2016) 69-78. https://doi.org/10.1016/j.optlastec.2016.07.001

[65] S. Sun, Y. Durandet, M. Brandt, Parametric investigation of pulsed Nd: YAG laser cladding of stellite 6 on stainless steel, Surface and Coatings Technology 194(2) (2005) 225-231. https://doi.org/10.1016/j.surfcoat.2004.03.058

[66] B. Budiansky, R.J. O'Connell, Elastic moduli of a cracked solid, International Journal of Solids and Structures 12(2) (1976) 81-97. https://doi.org/10.1016/0020-7683(76)90044-5

[67] Y. Javadi, M. Ashoori, Sub-surface stress measurement of cross welds in a dissimilar welded pressure vessel, Materials & Design 85 (2015) 82-90. https://doi.org/10.1016/j.matdes.2015.07.012

[68] Y. Javadi, K. Azari, S.M. Ghalehbandi, M.J. Roy, Comparison Between Using Longitudinal and Shear Waves in Ultrasonic Stress Measurement to Investigate the Effect of Post-Weld Heat-Treatment on Welding Residual Stresses, Research in Nondestructive Evaluation 28(2) (2017) 101-122. https://doi.org/10.1080/09349847.2015.1123786

[69] V. Fallah, M. Alimardani, S.F. Corbin, A. Khajepour, Impact of localized surface preheating on the microstructure and crack formation in laser direct deposition of Stellite 1 on AISI 4340 steel, Applied Surface Science 257(5) (2010) 1716-1723. https://doi.org/10.1016/j.apsusc.2010.09.003